

Group IV semiconductor Ge integration with topological insulator Sb_2Te_3 for spintronic application

This content has been downloaded from IOPscience. Please scroll down to see the full text.

2017 J. Phys. D: Appl. Phys. 50 105303

(<http://iopscience.iop.org/0022-3727/50/10/105303>)

View [the table of contents for this issue](#), or go to the [journal homepage](#) for more

Download details:

IP Address: 49.140.190.244

This content was downloaded on 03/03/2017 at 06:25

Please note that [terms and conditions apply](#).

You may also be interested in:

[Interfaces between CdS, CdTe and MoTe₂, WSe₂](#)

T Löher, Y Tomm, C Pettenkofer et al.

[Chemical and electronic properties of Fe/MgO/Ge heterostructures for spin electronics](#)

D Petti, M Cantoni, C Rinaldi et al.

[Hot wall epitaxy of topological insulator films](#)

Y Takagaki, B Jenichen, U Jahn et al.

[Molecular beam epitaxial growth and electronic transport properties of high quality topological insulator Bi₂Se₃ thin films on hexagonal boron nitride](#)

Joon Young Park, Gil-Ho Lee, Janghyun Jo et al.

[Characterization of MgO Thin Films Grown on Carbon Materials by Molecular Beam Epitaxy](#)

Satoshi Kobayashi, Shinji Miwa, Frédéric Bonell et al.

[Epitaxial Heusler alloy Co₂FeSi films on Si\(111\) substrates grown by molecular beam epitaxy](#)

M Zander, J Herfort, K Kumakura et al.

[Binary group III-nitride based heterostructures: band offsets and transport properties](#)

Basanta Roul, Mahesh Kumar, Mohana K Rajpalke et al.

[Pulsed laser deposition of La_{1-x}Sr_xMnO₃: thin-film properties and spintronic applications](#)

Sayani Majumdar and Sebastiaan van Dijken

[Spintronic oxides grown by laser-MBE](#)

Matthias Opel

Group IV semiconductor Ge integration with topological insulator Sb_2Te_3 for spintronic application

Beining Zheng, Yu Sun, Jie Wu, Mei Han, Xiaofeng Wu, Keke Huang and Shouhua Feng¹

State Key Laboratory of Inorganic Synthesis and Preparative Chemistry, College of Chemistry, Jilin University, Changchun 130012, People's Republic of China

E-mail: shfeng@jlu.edu.cn

Received 30 August 2016, revised 10 December 2016

Accepted for publication 8 January 2017

Published 10 February 2017



Abstract

$\text{Sb}_2\text{Te}_3/\text{Ge}$ heterojunctions were grown on deoxidized GaAs (001) substrates by molecular beam epitaxy to explore a new type of spin torque device. Despite the large lattice mismatch between Ge and Sb_2Te_3 , the films display highly uniform fabrication and good crystallinity, which have been confirmed by structural characterization. The band structures of $\text{Sb}_2\text{Te}_3/\text{Ge}$ heterojunctions were investigated by x-ray photoemission spectroscopy and ultraviolet photoemission spectroscopy. Small chemical shift of Sb 3d_{5/2} indicates that TI conducting surface is not destroyed, and Ge valence band bending contributes to Fermi level depinning. The band offset of $\text{Sb}_2\text{Te}_3/\text{Ge}$ heterojunctions is different from common gate dielectric/Ge heterojunctions. The integral quality of the heterostructure reveals the potential of combining topological insulators with semiconductors for the advancement of spintronic devices.

Keywords: topological insulator, Ge, heterojunction, molecular beam epitaxy, band alignment

 Supplementary material for this article is available [online](#)

(Some figures may appear in colour only in the online journal)

1. Introduction

Achieving efficient spin injection from ferromagnets into semiconductors is a challenging task in spintronics [1, 2]. Compared with Si, group IV semiconductor Ge possesses higher carrier mobility and faster spin relaxation, so it attracts tremendous attention as a spin channel material [3, 4]. Theoretically, the inverse spin-Hall effect in Ge-based heterostructures, which is originated from large spin-orbit interaction, can be spin-manipulative by Rashba field [5]. Inspiringly, the spin transport with diffusion lengthening out to $\lambda = 660 \pm 200$ nm at room temperature was demonstrated in epitaxial n-Ge layers [6]. However, the critical obstacles for efficient spin injection with Ge channel involve the conductivity mismatch and the strong Fermi-level pinning at metal/Ge interface [7–9]. An alternative approach is to insert a tunnel barrier

layer to tailor the contact interface [10]. Topological insulators (TIs) which possess conducting surface states but behave as insulators in the bulk are promising candidates for replacing Schottky contact [11]. The spin-momentum locking surface states of TI can generate pure spin-polarized currents and govern their amplitude and direction [12]. Another remarkable feature of TI is providing giant spin-transfer torque to an adjacent ferromagnet which results in spin current effective conversion [13]. As an intrinsic TI, Sb_2Te_3 is the existence of a metallic surface state within the bulk bandgap (~ 0.3 eV) [14, 15]. Sb_2Te_3 is suggested to be as an ideal tunnel barrier in ferromagnetic metal/semiconductor device for implementation of spin-polarized carriers injection and transport [16]. Therefore, monolithic integration of TI Sb_2Te_3 and Group IV semiconductor Ge is imperative for future spin-based applications.

Various substrate materials and surfaces such as graphene/SiC [17], Si [18, 19], $\text{SiO}_2/\text{BaF}_2$ [20], GaAs [21], and sapphire [22] have been reported for the epitaxial growths of Sb_2Te_3 ,

¹ Author to whom any correspondence should be addressed.

but the growth of $\text{Sb}_2\text{Te}_3/\text{Ge}$ heterojunctions by molecular beam epitaxy has not been found to the best of our knowledge. Furthermore, the band alignment properties play a dominant role in understanding spin transport behaviours of heterostructure barrier tunnelling [23]. Significant researches were conducted on the band alignment of high- κ gate dielectrics such as HfO_2 [24], Al_2O_3 [25], and BaTiO_3 [26] with respect to Ge. However, owing to the unique metallic Dirac surface states, the band values coupling Sb_2Te_3 to Ge are different from these native oxides. The fact of whether topological surface still exists needs to be confirmed. Ge surface state which is the origin of Fermi level pinning also needs to be examined [27]. Therefore, the band alignment between Sb_2Te_3 and Ge is essential to be provided when aiming at improving spintronic device.

In this work, we reported MBE growth of Sb_2Te_3 on Ge for high performance device configurations. The growth of Sb_2Te_3 thin film was achieved on Ge (001) layer despite that they have the very different crystal symmetries along the film growth direction. Moreover, there is no intermediate interlayer between Sb_2Te_3 and Ge films. We investigated the band alignment at $\text{Sb}_2\text{Te}_3/\text{Ge}$ heterointerface using x-ray photoelectron spectroscopy (XPS) and ultraviolet photoemission spectroscopy (UPS) measurement. No chemical shift of $\text{Sb } 3d_{5/2}$ reflects the weak bonding nature at $\text{Sb}_2\text{Te}_3/\text{Ge}$ interface as expected. The bending that Ge valence band departed from Fermi level was also observed. The measured value of valence and conduction band offset, ΔE_V and ΔE_C , are 0.25 ± 0.1 and 0.07 ± 0.11 eV, respectively. The properties are different from common gate dielectric due to the exotic conducting surface states of TI. The successful formation of $\text{Sb}_2\text{Te}_3/\text{Ge}$ interface is an essential step towards TIs based functional junctions.

2. Experimental

$\text{Sb}_2\text{Te}_3/\text{Ge}$ heterostructures were grown by MBE in a SVTA system equipped with Ge effusion cell and Te, Sb valved cracker cells in ultrahigh vacuum condition which was about 1×10^{-10} torr background pressure. Prior to growth, GaAs (001) wafers were heated up to 350 °C for surface deoxidation after degreasing. The Ge epilayers were deposited for 1 h at 330 °C. For the growth of Sb_2Te_3 films, high-purity Sb and Te sources were evaporated through pyrolysis heating and valves controlling, providing a beam flux Sb/Te ratio of about 2:3. The substrate temperature was kept at 200 °C throughout the Sb_2Te_3 growth. The growth rate was 0.38 nm min^{-1} . The films with different thicknesses were obtained by controlling growth time. A reflection high energy electron diffraction (RHEED) setup was attached to the MBE system for *in situ* monitoring the reconstruction and growth.

Structure and crystallinity of the heterostructures were characterized by SIEMENS D 5005 x-ray diffractometer including $\theta - 2\theta$ scans and ω scans. Atomic force microscopy (AFM) images were generated by Veeco Multimodel NanoScope 3D in the tapping mode. Transmission electron microscope (TEM) cross-sectional specimens were prepared by focused ion beam ablating in a FEI Helios NanoLab 600i

system. TEM study was carried out to characterize the interfaces between Sb_2Te_3 and Ge epilayers in a Hitachi H-8100 TEM. The Raman spectra were measured in the back scattering geometry in a DAC T64000 spectrograph system. And a solid-state, diode pumped, frequency-doubled Nd: vanadate laser ($\lambda = 532 \text{ nm}$) was used as excitation laser. Core level spectra of these samples were recorded by a Thermo Scientific ESCALAB 250Xi XPS system with a monochromated $\text{Al K}\alpha$ (1486.6 eV) x-ray source. The valence bands (VB) of these individual layers of heterostructures were recorded by a PREVAC UPS system under He irradiation ($h\nu = 21.2 \text{ eV}$). Fourier transform infrared spectroscopy (FT-IR) absorption spectrum was performed on a Bruker IFS 66 V/S IR spectrometer. The single Ge layer and 1 h growth Sb_2Te_3 film was investigated to get their absorbance spectrum. Prior to the measurement, the spectrometer was purged with CO_2 air. The samples were fixed on the holder of the instrument. For each sample, 102 scans with a resolution of 4 cm^{-1} were taken for spectrum integration in the wavenumber range from 4000 to 400 cm^{-1} .

3. Results and discussion

The growth of $\text{Sb}_2\text{Te}_3/\text{Ge}$ heterostructure was monitored *in situ* by RHEED. The clean GaAs (001) surface was observed by *in situ* RHEED in figure 1(a). The (2×1) reconstructed Ge surface which maintained GaAs (001) primary diffraction streaks is shown in figure 1(b) because of the similar lattice parameters between Ge and GaAs. The formation of this RHEED pattern reflecting the epitaxial character of Ge growth is the same as previously reported [28]. The Sb_2Te_3 RHEED patterns with different growth time are shown in figures 1(c) 5 min and (d) 1 h. Despite the large lattice mismatch of about 24% between Ge (001) and Sb_2Te_3 (001), it is noted that the initial crystalline Sb_2Te_3 pattern was immediately textured and sharp streaky RHEED patterns show the yielding of smooth epitaxial hetero-interface [18]. Although the diffraction pattern confirms a typical crystalline growth, the presence of faint streaks suggest that Sb_2Te_3 films may have formed a twin structure, which was observed by other group previously [29]. Furthermore, the additional streaks are caused by the 30° rotation domains which were observed by scanning tunneling microscope [30].

The structural properties of $\text{Sb}_2\text{Te}_3/\text{Ge}$ heterostructure were obtained by a x-ray diffraction (XRD) and AFM. The crystal structure and orientation are shown in figure 2(a). The intense coincident peaks of Ge (004) and GaAs (004) with a full width half maximum (FWHM) of 0.01° indicate high crystalline quality of Ge epitaxial film. For Sb_2Te_3 films, XRD profiles reveal that these reflections are generated only from (003)-type lattice planes. All peaks could be indexed to rhombohedral phase (Inorganic Crystal Structure Database Minerals 15-0874, $R\bar{3}m$). These manifest that Sb_2Te_3 films are highly *c*-axis perpendicular to the substrate surface. The FWHM of rocking curve for Sb_2Te_3 (006) reflection is 0.6596° and for (009) is 0.2213° , as shown in figures 2(b) and (c). The Sb_2Te_3 dominant defects are tellurium vacancies and antisite defects

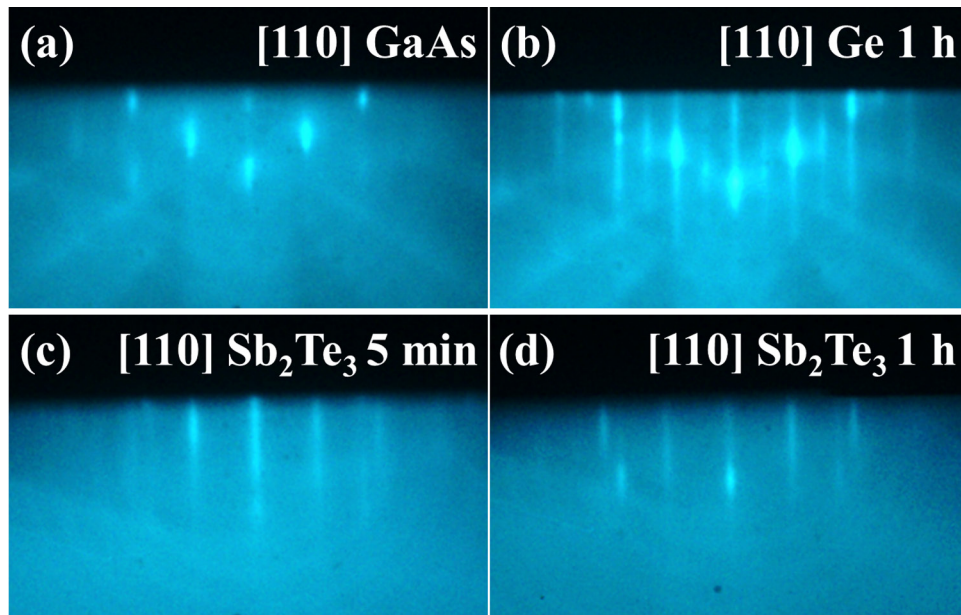


Figure 1. Evolution of RHEED pattern during the growth of $\text{Sb}_2\text{Te}_3/\text{Ge}$ heterostructures on GaAs (001). (a) GaAs (001) substrate after 5 min annealing at 350 °C, (b) Ge film with 1 h growth on GaAs at 330 °C, (c), (d) Sb_2Te_3 films with 5 min growth and 1 h growth on Ge/GaAs (001) at 200 °C, respectively. The incidence azimuth of the electron beam in all RHEED patterns is along [1 1 0] direction.

[31]. And these defects can donate charges so they have significant influence on the electronic transport property. In this case, although the molecular beam epitaxy is efficient to avoid defect formation, the existence defects are still proved in the structure by the Sb_2Te_3 RHEED pattern and rocking curve reflection. The growth with fewer vacancy and antisite defects can be achieved by controlling the growth conditions. Additionally, the surface morphologies of the samples are exhibited in figures 2(d)–(f). The corresponding average roughness (R_a) and root-mean-square roughness (R_q) for a single Ge film are 1.36 and 1.72 nm, for 5 min $\text{Sb}_2\text{Te}_3/\text{Ge}$ are 0.687 and 0.936 nm, and for 1 h $\text{Sb}_2\text{Te}_3/\text{Ge}$ are 0.662 and 0.849 nm. It suggests that the rough Ge film surface tends to be flat after a growth of 2 quintuple layers (QLs) Sb_2Te_3 . The significant variation in roughness gives an indirect evidence for a natural layer-by-layer growth mode of TI films. Such TI planar characteristic is suitable for size-controllable integrated devices.

Cross-sectional high resolution transmission electron microscopy (HR-TEM) was used to characterize the interface of $\text{Sb}_2\text{Te}_3/\text{Ge}$ heterostructure. For this purpose, the electron transparent foil of $\text{Sb}_2\text{Te}_3/\text{Ge}/\text{GaAs}$ (001) sample was prepared using focused ion beam. Pt deposition and a Gallium ions beam were employed to ablate very narrow (<100 nm thick) upstanding slice. The height profile across the complete plane is shown in figure 3(a) in which the uniform thickness of Sb_2Te_3 and Ge layers could be observed in a long range. Selected area electron diffraction (SAED) pattern of Sb_2Te_3 is a superposition of the Ge and GaAs patterns as shown in figure 2(b). SAED patterns confirm that the c -axis orientation of Sb_2Te_3 film lies along either $[\bar{1} 1 0]$ or $[1 1 0]$ direction on the Ge epilayer surface. Figure 3(c) shows the $\text{Sb}_2\text{Te}_3/\text{Ge}$ interface in detail. The partial enlarged HR-TEM image of $\text{Sb}_2\text{Te}_3/\text{Ge}$ heterostructure and HR-TEM micrograph for the Ge/GaAs interfaces are shown in the supporting information (figures S1 and S2 (stacks.iop.org/JPhysD/50/105303/mmedia)).

The highly structure-perfection of parallel QL is confirmed. The atomic structure is schematically shown in figure 3(d). The sharp heterointerface between Ge (001) and Sb_2Te_3 (001) is formed and the strain is relaxed rapidly. The unique feature could attribute to the weak van der Waals epitaxy [32] and was observed at other TI heterointerfaces [33–35]. Moreover, there is no unwanted interlayer diffusion in $\text{Sb}_2\text{Te}_3/\text{Ge}$ interface [36, 37]. This consequence could give rise to minimizing the interface scattering of carrier transport from tunnel barrier to the semiconductor [38] and is in favour of better electrical transport characteristics for low-power spintronic applications.

Figure 4 shows typical Raman spectra of $\text{Sb}_2\text{Te}_3/\text{Ge}$ heterostructures. Prior to the measurement, the spectrometer was calibrated using a Si line. The green curve is for 5 min deposited Sb_2Te_3 obtained under exciting power 50 mW. In order to achieve longer penetration depth, higher excitation power of 150 mW was employed for 1 h Sb_2Te_3 sample (red curve). The peaks of 5 min Sb_2Te_3 which thickness is about 2 QL could still be observed despite of weakness. For the 1 h Sb_2Te_3 sample, the peaks become more evident. The strong peak located at 301.2cm^{-1} is corresponding to Ge film [39]. The other five peaks could be identified as Sb_2Te_3 film and are consistent with the result reported earlier [40]. The peaks located at 72.6 , 123.2 and 165.4cm^{-1} among them are in agreement with the characteristic peaks of the Sb_2Te_3 single crystal. Named as A_{1g}^1 , E_g^2 and A_{1g}^2 modes respectively, the peaks were determined experimentally and also calculated in the previous work (the subscript ‘g’ denotes Raman active modes, E and A represent the in-plane and out-of plane lattice vibrations, respectively) [41, 42]. The additional peaks are denoted as P_1 and P_2 . P_1 is probably an infrared-active mode of the Sb_2Te_3 film named Au (‘u’ denotes IR-active modes) which could be detected under resonance excitation conditions due to the very strong electron coupling to the electric field produced by

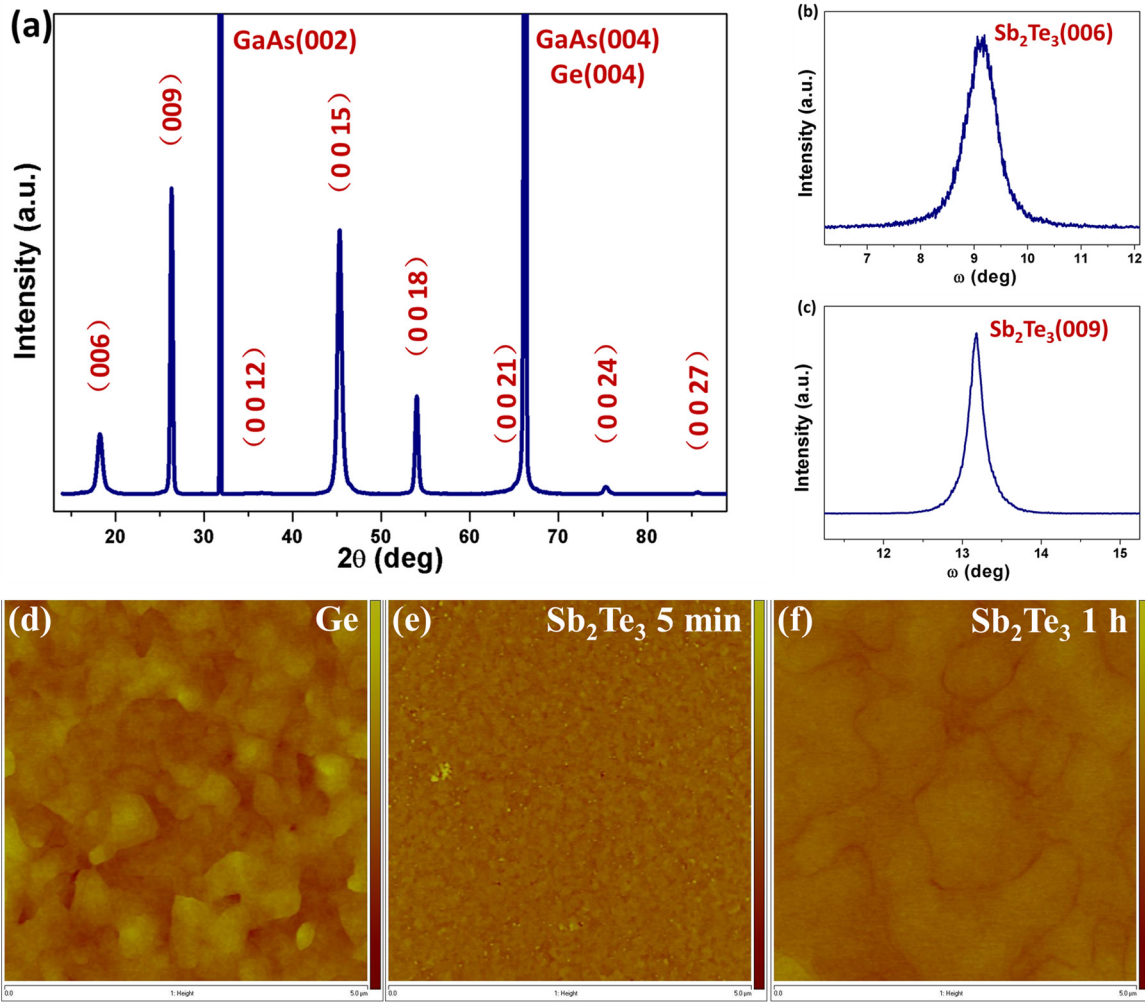


Figure 2. (a) XRD patterns of as-grown $\text{Sb}_2\text{Te}_3/\text{Ge}$ heterostructure, (b) and (c) the rocking curves of Sb_2Te_3 (006), (009) peaks. (d)–(f) AFM images for the single Ge flim with 1 h growth, Sb_2Te_3 films with 5 min and 1 h growth, respectively. The scanning area in each figure is $5 \times 5 \mu\text{m}$ and the right side pillars are z scale bar with the maximum 20 nm for the height distribution.

longitudinal optical phonons [43]. However, the origin of P_2 is still unknown and needs further study.

In order to determine ΔE_V and ΔE_C at $\text{Sb}_2\text{Te}_3/\text{Ge}$ hetero-interface, core level binding energies and valance band maximum (VBM) values were measured by XPS and UPS. These measurements were performed on the following 3 samples: (1) single Ge epitaxial layer (1 h growth), (2) 23 nm thick Sb_2Te_3 film (1 h growth) on Ge layer, and (3) the thickness less than 2 nm Sb_2Te_3 film (5 min growth) on Ge layer. The binding energy was corrected by adjusting the C 1s core-level peak position to 284.6 eV for each sample. The position of Sb 3d_{5/2} peak centroid from XPS measurement is found to be 528.70 ± 0.05 eV as shown in figure 5(a). The high intensity of Sb–O peaks is attributed to that Sb_2Te_3 is easily oxidized in atmosphere and Sb element is easy to be oxidized [44, 45]. Through the peak fitting procedure, the positions of Sb 3d peaks centroid don't shift compared with the etching results which are shown in the supporting information (figure S3). There is no influence on the band offset value selecting Sb 3d_{5/2} core level or Sb 3d_{3/2} since the binding energy separation between their peaks is fixed to be 9.35 eV. The Sb_2Te_3 UPS spectrum is depicted in figure 5(a). The VBM value is

determined by extrapolating linearly the leading edge to the extended base line of VB spectra [46, 47]. The VBM position of Sb_2Te_3 is estimated as 0.23 eV below the Fermi level. Therefore the energy difference between Sb 3d_{5/2} centroid and Sb_2Te_3 VBM is measured to be 528.47 ± 0.05 eV. With the same method, Ge 3d and Ge VBM spectra are recorded in figure 5(b), and the energy difference between Ge 3d centroid and Ge VBM is found to be 29.57 ± 0.05 eV for single Ge film. In figure 5(c), the presence of the peak located at 32.6 eV for Ge 3d on the hetero-interface of $\text{Sb}_2\text{Te}_3/\text{Ge}$ is typical Ge–O bonding [48]. The peak position is completely identical with single Ge sample, and compared to the single Ge layer, the Ge–O peak intensity enhancement can be attributed to thin Sb_2Te_3 covering layer on the Ge surface. The energy difference between Sb 3d_{5/2} centroid and Ge 3d centroid is determined to be 498.70 ± 0.05 eV. The ΔE_V at the $\text{Sb}_2\text{Te}_3/\text{Ge}$ hetero-interface is determined by these measured core levels and VBM spectra with the following equation [49]:

$$\Delta E_V = (E_{\text{Sb } 3d}^{\text{Sb}} - E_{\text{VBM}}^{\text{Sb}})^{\text{1h } \text{Sb}_2\text{Te}_3} - (E_{\text{Ge } 3d}^{\text{Ge}} - E_{\text{VBM}}^{\text{Ge}})^{\text{Ge}} - (E_{\text{Sb } 3d}^{\text{Sb}} - E_{\text{Ge } 3d}^{\text{Ge}})^{\text{5 min } \text{Sb}_2\text{Te}_3/\text{Ge interface}} \quad (1)$$

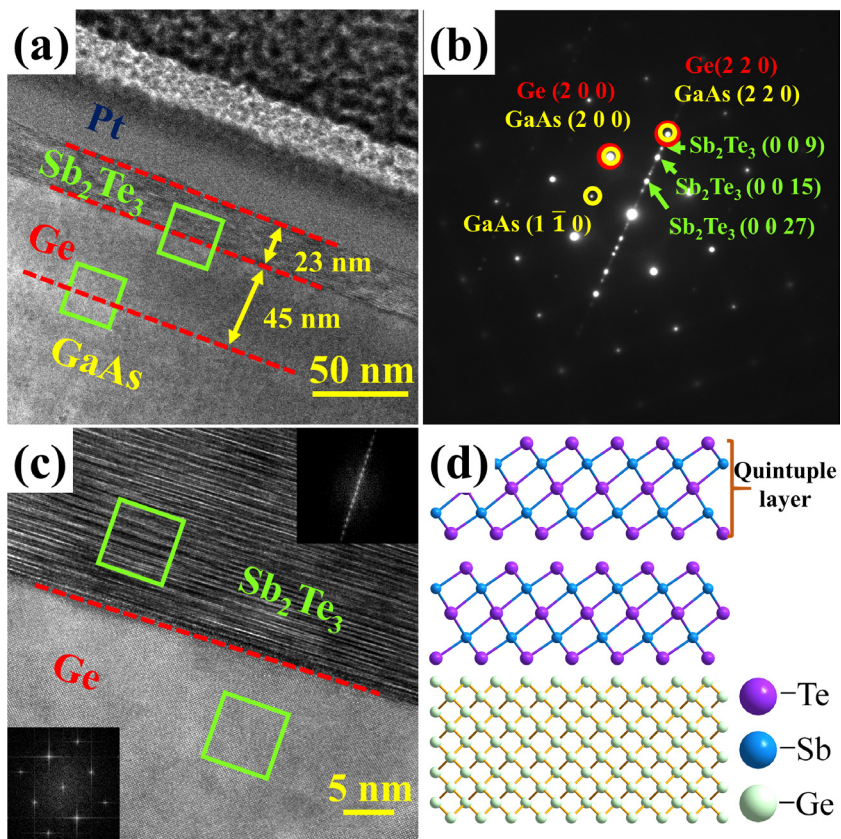


Figure 3. (a) Cross-sectional HR-TEM images of $\text{Sb}_2\text{Te}_3/\text{Ge}/\text{GaAs}$ (001) integral structure. (b) SAED pattern taken along [100] Sb_2Te_3 orientation. Sb_2Te_3 and Ge/GaAs diffraction indices are marked in the graph. (c) HR-TEM micrograph for $\text{Sb}_2\text{Te}_3/\text{Ge}$ interfaces. The insets show the Fourier-transform diffractograms of the segment joints. (d) Atomic structure of the heterostructure, with Ge abutted by Sb_2Te_3 (only 2 QL is shown for simplicity). The horizontal axis is along the [111] direction. The color scheme here is Te (purple), Sb (blue), and Ge (green).

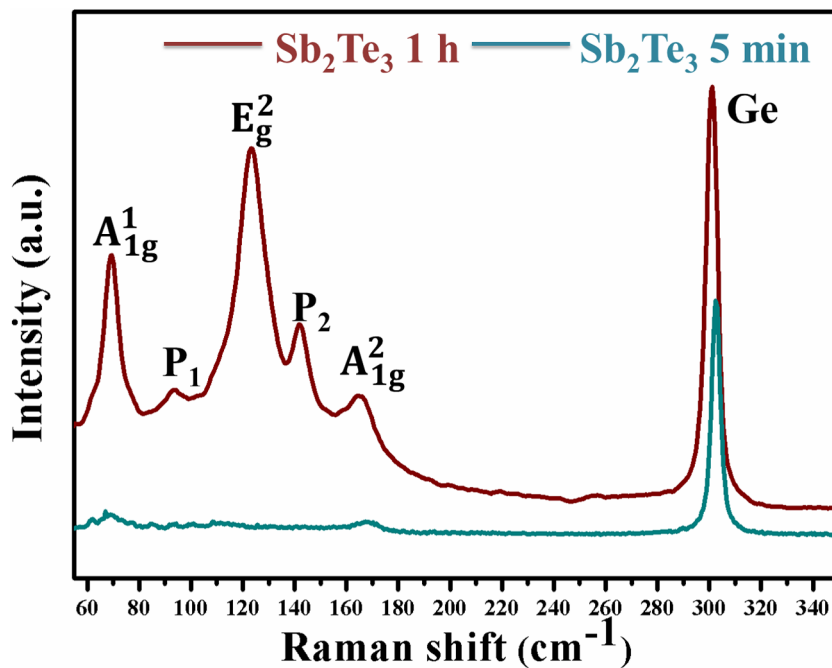


Figure 4. The Raman spectra of $\text{Sb}_2\text{Te}_3/\text{Ge}$ heterostructures collected from Sb_2Te_3 films with 1 h growth (red curve) and 5 min growth (green curve). The spectra were obtained at room temperature with 532 nm excitation.

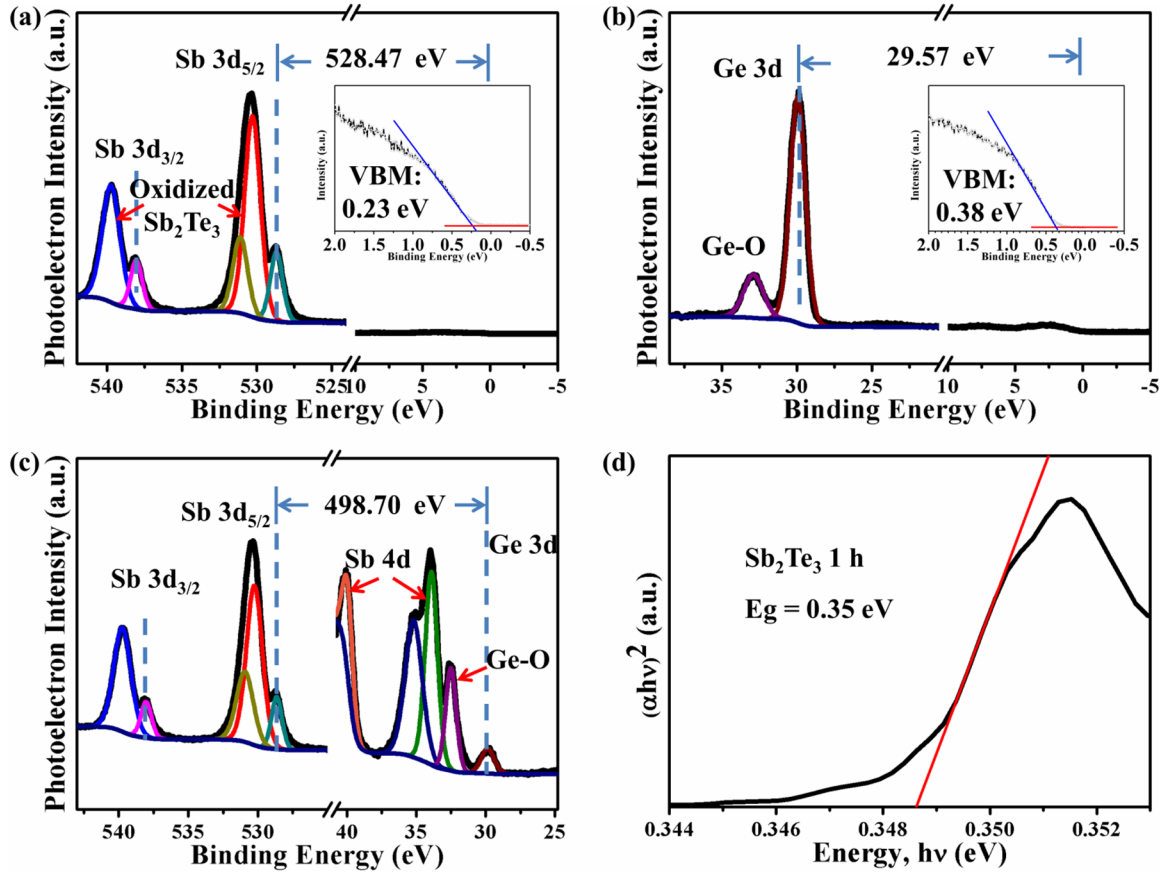


Figure 5. (a) Sb 3d core level ($E_{\text{Sb } 3d}^{\text{Sb}}$) and VBM ($E_{\text{VBM}}^{\text{Sb}}$) of Sb_2Te_3 film with 1 h deposited, (b) Ge 3d core level ($E_{\text{Ge } 3d}^{\text{Ge}}$) and VBM ($E_{\text{VBM}}^{\text{Ge}}$) of single Ge film, (c) Sb 3d core level ($E_{\text{Sb } 3d}^{\text{Sb}}$) and Ge 3d core level ($E_{\text{Ge } 3d}^{\text{Ge}}$) of 5 min deposited Sb_2Te_3 film/Ge interface. (d) Absorption coefficient of the band gap of Sb_2Te_3 was determined showed the core level spectrum of Sb_2Te_3 film with 1 h deposited. The Sb_2Te_3 band gap of 0.3 eV was determined from this plot.

Substituting the respective XPS and UPS data in the equation, we obtain ΔE_V of $\text{Sb}_2\text{Te}_3/\text{Ge}$ heterostructure as 0.25 ± 0.1 eV. Furthermore, ΔE_C at $\text{Sb}_2\text{Te}_3/\text{Ge}$ heterointerface is determined from the following equation:

$$\Delta E_C = E_g^{\text{Ge}} - E_g^{\text{Sb}_2\text{Te}_3} - \Delta E_V \quad (2)$$

The band gap of Sb_2Te_3 is precisely determined by absorption coefficient measurement. As $(\alpha h\nu)^2 = A(h\nu - E_g)$ [50], where E_g is the band gap energy, A is a constant and $h\nu$ is the incident photon energy, α is the absorption coefficient. The Sb_2Te_3 and Ge/GaSb absorption coefficients are shown in the supporting information (figure S4). Figure 5(d) shows the $(\alpha h\nu)^2$ versus $h\nu$ curve. The Sb_2Te_3 band gap energy $\sim 0.35 \pm 0.01$ eV is determined by extrapolating the linear part of the data to the x axis of the curve. The ΔE_C is calculated to be 0.07 ± 0.11 eV by the measured value of ΔE_V , the measured bandgap of Sb_2Te_3 , and the bandgap of Ge 0.67 eV. The core level to VBM binding-energy difference and the resulting band offsets on Ge (100) epitaxial layer are tabulated in table 1.

We observe binding energy shifts between Sb $3d_{5/2}$ and Ge 3d core levels in each thin film sample and the same core levels in heterostructure sample, which show the band bending at the heterointerface. Binding energy shifts are

Table 1. Core-level to VBM binding energy difference for Sb_2Te_3 and Ge layer.

Material and interface	Binding energy difference	Measured band offset of the $\text{Sb}_2\text{Te}_3/\text{Ge}$ heterostructure	
		ΔE_V	ΔE_C
Sb_2Te_3	$E_{\text{Sb } 3d}^{\text{Sb}} - E_{\text{VBM}}^{\text{Sb}} = 528.47 \pm 0.05$ eV	—	—
Ge	$E_{\text{Ge } 3d}^{\text{Ge}} - E_{\text{VBM}}^{\text{Ge}} = 29.57 \pm 0.05$ eV	—	—
$\text{Sb}_2\text{Te}_3/\text{Ge}$ interface	$E_{\text{Ge } 3d}^{\text{Ge}} - E_{\text{Sb } 3d}^{\text{Sb}} = 498.70 \pm 0.05$ eV	0.25 ± 0.1 eV	0.07 ± 0.11 eV
Eg of Sb_2Te_3	0.35 ± 0.01 eV	—	—

found to be $528.70 - 528.70 = 0$ eV for Sb $3d_{5/2}$ peak and $30.05 - 29.95 = 0.10$ eV for Ge 3d peak. The results reflect the weak bonding between Sb_2Te_3 epilayer and Ge surface. It is a consequence of van der Waals nature of TIs [46]. A schematic band diagram for the $\text{Sb}_2\text{Te}_3/\text{Ge}$ hetero-structure is constructed using these band offset values, band bending and band gaps (shown in figure 6). These results would allow us to tune the Fermi level to the Dirac point and to control spin polarization in TI [51, 52]. And in this case, Ge valence band

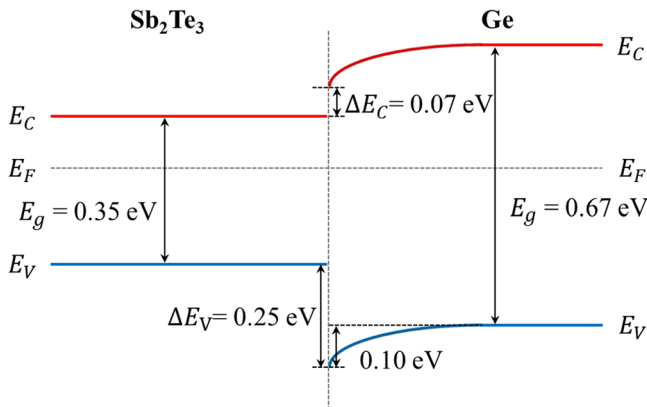


Figure 6. Energy-band diagram of $\text{Sb}_2\text{Te}_3/\text{Ge}$ heterojunction.

bends away from the Fermi-level [8], probably because of weak interfacing with the Sb_2Te_3 exotic cone-shaped gapless surface state. For the electrical transport on the energy-band diagram which we constructed, we expect that the out-of-plane resistivity would achieve further increase in transistor drive current and minimize the gate leakage; the exotic TI spin texture in-plane could lead to a current-induced spin polarization in the surface states [52]. These effects would enhance the spin injection efficiency, however it still need direct proof via electronic and spin injection measurements.

4. Conclusions

In conclusion, $\text{Sb}_2\text{Te}_3/\text{Ge}$ heterostructures were successfully grown on GaAs (001) substrates by MBE method. For layer-by-layer epitaxial growth, the films are highly uniform and with good crystallinity confirmed by structural and topographic properties. Cross-sectional HR-TEM shows a sharp heterointerface and the different crystal symmetries of the two materials. Raman mapping confirms the presence of strong characteristic peaks reported previously for these materials in bulk form. Based on precise XPS and UPS measurements, no chemical shift of Sb_2Te_3 reflects that TI conduction state was conserved. The Ge valence band bending demonstrates that inserting thin TI tunnel barriers could solve the problem of Fermi level pinning close to the Ge valence band at metal/Ge junctions. The valence and conduction band offsets of Sb_2Te_3 with respect to Ge are measured as 0.25 ± 0.1 and 0.07 ± 0.11 eV. The schematic band diagram for $\text{Sb}_2\text{Te}_3/\text{Ge}$ heterojunction is proposed. These properties show significant difference from common gate dielectric and would offer support for further study on their distinct electrical transport properties. Considering the van der Waals layered characteristics of TIs sharing similar crystal structure of Sb_2Te_3 , our results should be possible to serve as useful reference for integration of other TIs and Ge-based semiconductor for spintronic applications.

Acknowledgments

This work was supported by the National Natural Science Foundation of China (Grants 21427802, 21131002 and 21201075).

References

- [1] Zutic I, Fabian J and Sarma S 2004 Spintronics: fundamentals and applications *Rev. Mod. Phys.* **76** 323
- [2] Awschalom D D and Flatté M E 2007 Challenges for semiconductor spintronics *Nat. Phys.* **3** 153
- [3] Sze S M and Ng K K 2006 *Physics of Semiconductor Devices* (New York: Wiley)
- [4] Zhou Y, Han W, Chang L T, Xiu F X, Wang M S, Oehme M, Fischer I A, Schulze J, Kawakami R K and Wang K L 2011 Electrical spin injection and transport in germanium *Phys. Rev. B* **84** 125323
- [5] Jain A et al 2015 Crossover from spin accumulation into interface states to spin injection in the germanium conduction band *Phys. Lett.* **109** 106603
- [6] Dushenko S, Koike M, Ando Y, Shinjo T, Myronov M and Shiraishi M 2015 Experimental demonstration of room-temperature spin transport in n-type germanium epilayers *Phys. Rev. Lett.* **114** 196602
- [7] Fert A and Jaffres H 2001 Conditions for efficient spin injection from a ferromagnetic metal into a semiconductor *Phys. Rev. B* **64** 184420
- [8] Dimoulas A, Tsipas P, Sotiropoulos A and Evangelou E K 2006 Fermi-level pinning and charge neutrality level in germanium *Appl. Phys. Lett.* **89** 252110
- [9] Nishimura T, Kita K and Toriumi A 2007 Evidence for strong Fermi-level pinning due to metal-induced gap states at metal/germanium interface *Appl. Phys. Lett.* **91** 123123
- [10] Friedman A L, Erve O M J, Li C H, Robinson J T and Jonker B T 2014 Homoepitaxial tunnel barriers with functionalized graphene-on-graphene for charge and spin transport *Nat. Commun.* **5** 3161
- [11] Hasan M Z and Kane C L 2010 Colloquium: topological insulators *Rev. Mod. Phys.* **82** 3045
- [12] Vaklinova K, Hoyer A, Burghard M and Kern K 2016 Current-induced spin polarization in topological insulator-graphene heterostructures *Nano Lett.* **16** 2595
- [13] Mellnik A R et al 2014 Spin-transfer torque generated by a topological insulator *Nature* **511** 449
- [14] Zhu S Y et al 2015 Ultrafast electron dynamics at the Dirac node of the topological insulator Sb_2Te_3 *Sci. Rep.* **5** 13213
- [15] Hsieh D et al 2009 Observation of time-reversal-protected single-Dirac-cone topological-insulator states in Bi_2Te_3 and Sb_2Te_3 *Phys. Rev. Lett.* **103** 146401
- [16] Chang J, Register L F and Banerjee S K 2012 Topological insulator Bi_2Se_3 thin films as an alternative channel material in metal-oxide-semiconductor field-effect transistors *J. Appl. Phys.* **112** 124511
- [17] Jiang Y P, Wang Y L, Chen M, Li Z, Song C L, He K, Wang L L, Chen X, Ma X C and Xue Q K 2012 Landau quantization and the thickness limit of topological insulator thin films of Sb_2Te_3 *Phys. Rev. Lett.* **108** 016401
- [18] Wang G A 2010 Atomically smooth ultrathin films of topological insulator Sb_2Te_3 *Nano Res.* **3** 874
- [19] Zhang X P, Zeng Z G, Shen C, Zhang Z Q, Wang Z C, Lin C and Hu Z Y 2014 Investigation on the electrical transport properties of highly (001)-textured Sb_2Te_3 films deposited by molecular beam epitaxy *J. Appl. Phys.* **115** 024307
- [20] Aabdin Z, Peranio N, Winkler M, Bessas D, König J, Hermann R P, Bottner H and Eibl O 2012 Sb_2Te_3 and Bi_2Te_3 thin films grown by room-temperature MBE *J. Electron. Mater.* **41** 1493
- [21] Zeng Z Q et al 2013 Molecular beam epitaxial growth of Bi_2Te_3 and Sb_2Te_3 topological insulators on GaAs (111) substrates: a potential route to fabricate topological insulator p-n junction *AIP Adv.* **3** 072112
- [22] Chien Y J, Zhou Z H and Uher C 2005 Growth and transport properties of $\text{Sb}_{2-x}\text{V}_x\text{Te}_3$ thin films on sapphire substrates *J. Cryst. Growth* **283** 309

- [23] Spicer W, Lindau I, Skeath P, Su C and Chye P 1980 Unified mechanism for Schottky-barrier formation and III–V oxide interface states *Phys. Rev. Lett.* **44** 420
- [24] Hudait M K and Zhu Y 2013 Energy band alignment of atomic layer deposited HfO₂ oxide film on epitaxial (1 0 0) Ge, (1 1 0) Ge, and (1 1 1) Ge layers *J. Appl. Phys.* **113** 114303
- [25] Swaminathan S, Sun Y, Pianetta P and McIntyre P C 2011 Ultrathin ALD-Al₂O₃ layers for Ge (0 0 1) gate stacks: local composition evolution and dielectric properties *J. Appl. Phys.* **110** 094105
- [26] Hudait M K, Zhu Y, Jain N, Maurya D, Zhou Y and Priya S 2013 Quasi-zero lattice mismatch and band alignment of BaTiO₃ on epitaxial (1 1 0) Ge *J. Appl. Phys.* **114** 024303
- [27] Zhou Y, Han W, Wang Y, Xiu F X, Zou J, Kawakami R K and Wang K L 2010 Investigating the origin of Fermi level pinning in Ge Schottky junctions using epitaxially grown ultrathin MgO films *Appl. Phys. Lett.* **96** 102103
- [28] Molle A, Lamagna L, Spiga S, Fanciulli M, Brammertz G and Meuris M 2010 Interface analysis of Ge ultra thin layers intercalated between GaAs substrates and oxide stacks *Thin Solid Films* **518** S123
- [29] Li H D, Wang Z Y, Kan X, Guo X, He H T, Wang Z, Wang J N, Wong T L, Wang N and Xie M H 2010 The van der Waals epitaxy of Bi₂Se₃ on the vicinal Si (1 1 1) surface: an approach for preparing high-quality thin films of a topological insulator *New J. Phys.* **12** 103038
- [30] Wang Z Y, Li H D, Guo X, Ho W K and Xie M H 2011 Growth characteristics of topological insulator Bi₂Se₃ films on different substrates *J. Cryst. Growth* **334** 96
- [31] Hu L, Zhu T, Liu X and Zhao X 2014 Point defect engineering of high-performance bismuth–telluride-based thermoelectric materials *Adv. Funct. Mater.* **24** 5211–8
- [32] Liu X, Smith D J, Fan J, Zhang Y H, Cao H, Chen Y P, Leiner J, Kirby B J, Dobrowolska M and Furdyna J K 2011 Structural properties of Bi₂Te₃ and Bi₂Se₃ topological insulators grown by molecular beam epitaxy on GaAs (0 0 1) substrates *Appl. Phys. Lett.* **99** 171903
- [33] Chen X, Ma X C, He K, Jia J F and Xue Q K 2011 Molecular beam epitaxial growth of topological insulators *Adv. Mater.* **23** 1162
- [34] Li H D, Wang Z Y, Guo X, Wong T L, Wang N and Xie M H 2011 Growth of multilayers of Bi₂Se₃/ZnSe: heteroepitaxial interface formation and strain *Appl. Phys. Lett.* **98** 043104
- [35] Richardella A, Zhang D M, Lee J S, Koser A, Rench D W, Yeats A L, Buckley B B, Awschalom D D and Samarth N 2010 Coherent heteroepitaxy of Bi₂Se₃ on GaAs (1 1 1) B *Appl. Phys. Lett.* **97** 262104
- [36] Yuan Z, Liu J, Weaver J, Chen C L, Jiang J C, Lin B, Giurgiutiu V, Bhalla A and Guo R Y 2007 Ferroelectric BaTiO₃ thin films on Ni metal tapes using NiO as buffer layer *Appl. Phys. Lett.* **90** 202901
- [37] Brossard S, Munroe P R, Tran A T T and Hyland M M 2010 Study of the microstructure of NiCr splats plasma sprayed on to stainless steel substrates by TEM *Surf. Coat. Technol.* **204** 1608–15
- [38] McKee R, Walker F and Chisholm M 1988 Crystalline oxides on silicon: the first five monolayers *Phys. Rev. Lett.* **81** 3014
- [39] Kolobov A V 2000 Raman scattering from Ge nanostructures grown on Si substrates: power and limitations *J. Appl. Phys.* **87** 2926
- [40] Goncalves L M, Alpuim P, Rolo A G and Correia J H 2011 Thermal co-evaporation of Sb₂Te₃ thin-films optimized for thermoelectric applications *Thin Solid Films* **519** 4152
- [41] Sosso G C, Caravati S and Bernasconi M 2009 Vibrational properties of crystalline Sb₂Te₃ from first principles *J. Phys.: Condens. Matter* **21** 095410
- [42] Richter W and Becker C 1977 A Raman and far-infrared investigation of phonons in the rhombohedral V₂-VI₃ compounds Bi₂Te₃, Bi₂Se₃, Sb₂Te₃ and Bi₂(Te_{1-x}Se_x)₃ (0 < x < 1), (Bi_{1-y}Sb_y)₂Te₃ (0 < y < 1) *Phys. Status Solidi b* **84** 619
- [43] Shahil K M F, Hossain M Z, Teweldebrhan D and Balandin A A 2010 Crystal symmetry breaking in few-quintuple Bi₂Te₃ films: applications in nanometrology of topological insulators *Appl. Phys. Lett.* **96** 153103
- [44] Cui H, Bhat I B and Venkatasubramanian R 1999 Optical constants of Bi₂Te₃ and Sb₂Te₃ measured using spectroscopic ellipsometry *J. Electron. Mater.* **28** 1111–4
- [45] Krachler M, Emons H and Zheng J 2001 Speciation of antimony for the 21st century: promises and pitfalls *TRAC Trends Anal. Chem.* **20** 79–90
- [46] Li H, Gao L, Li H, Wang G, Wu J, Zhou Z and Wang Z 2013 Growth and band alignment of Bi₂Se₃ topological insulator on H-terminated Si (1 1 1) van der Waals surface *Appl. Phys. Lett.* **102** 074106
- [47] Chambers S A, Droubay T, Kaspar T C and Gutowski M 2004 Experimental determination of valence band maxima for SrTiO₃, TiO₂, and SrO and the associated valence band offsets with Si (0 0 1) *J. Vac. Sci. Technol. B* **22** 2205–15
- [48] Cheng C H, Chen P C, Liu S L, Wu T L, Hsu H H, Chin A and Yeh F S 2011 Bipolar switching characteristics of low-power GeO resistive memory *Solid-State Electron.* **62** 90–3
- [49] Kraut E, Grant R, Waldrop J and Kowalczyk S 1980 Precise determination of the valence-band edge in x-ray photoemission spectra: application to measurement of semiconductor interface potentials *Phys. Rev. Lett.* **44** 1620
- [50] Kryukov A I, Zin'chuk N N, Korzhak A V and Kuchmii S Y 2001 Quantum size effects and nature of photoprocesses in nanoparticles of Ag₂S *Theor. Exp. Chem.* **37** 296–303
- [51] He X Y, Guan T, Wang X X, Feng B J, Cheng P, Chen L, Li Y Q and Wu K H 2012 Highly tunable electron transport in epitaxial topological insulator (Bi_{1-x}Sb_x)₂Te₃ thin films *Appl. Phys. Lett.* **101** 123111
- [52] Yazyev O V, Moore J E and Louie S G 2010 Spin polarization and transport of surface states in the topological insulators Bi₂Se₃ and Bi₂Te₃ from first principles *Phys. Rev. Lett.* **105** 266806